NANO LETTERS

Letter

pubs.acs.org/NanoLett

Direct Imaging of Charged Impurity Density in Common Graphene Substrates

Kristen M. Burson,[†] William G. Cullen,*[,†] Shaffique Adam,[‡,§] Cory R. Dean,[∥,⊥,■] K. Watanabe,[●] T. Taniguchi,[●] Philip Kim,[¶] and Michael S. Fuhrer[†,#]

[†]Center for Nanophysics and Advanced Materials, University of Maryland, College Park, Maryland 20742-4111, United States

[‡]Yale-NUS College, 6 College Avenue East, 138614, Singapore

[§]Graphene Research Centre and Department of Physics, National University of Singapore, 2 Science Drive 3, 117551, Singapore

[∥]Department of Electrical Engineering, and [⊥]Department of Mechanical Engineering and [¶]Department of Physics, Columbia University, New York, New York, 10027, United States

[■]Department of Physics, The City College of New York, New York, New York 10031, United States

[●]Advanced Materials Laboratory, National Institute for Materials Science, 1-1 Namiki, Tsukuba, 305-0044, Japan

[#]School of Physics, Monash University, Victoria 3800, Australia

ABSTRACT: Kelvin probe microscopy in ultrahigh vacuum is used to image the local electrostatic potential fluctuations above hexagonal boron nitride (h-BN) and SiO_2, common substrates for graphene. Results are compared to a model of randomly distributed charges in a two-dimensional (2D) plane. For SiO_2, the results are well modeled by 2D charge densities ranging from 0.24 to 2.7 × 10^{11} cm^{-2}, while h-BN displays potential fluctuations 1−2 orders of magnitude lower than SiO_2, consistent with the improvement in charge carrier mobility for graphene on h-BN compared to SiO_2. Electron beam exposure of SiO_2 increases the charge density fluctuations, creating long-lived metastable charge populations of ∼2 × 10^{11} cm^{-2} at room temperature, which can be reversed by heating.

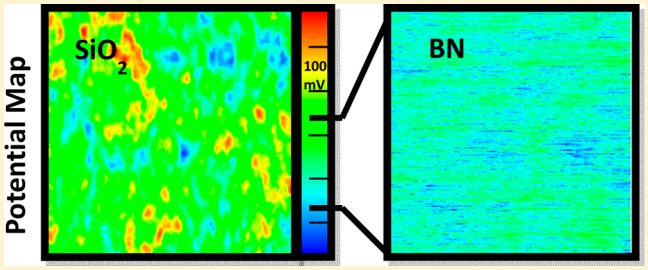

KEYWORDS: *Graphene, noncontact atomic force microscopy, Kelvin probe force microscopy, charged impurity scattering, charge inhomogeneity*

Graphene has attracted a great deal of attention due to its phenomenal electronic and mechanical properties.[1−3] Particularly notable is its high carrier mobility; graphene has the highest known intrinsic charge carrier mobility of any material at room temperature.[4] Exfoliated graphene devices that are suspended (i.e., no substrate) or placed on hexagonal boron nitride (h-BN) substrates have shown low-temperature mobilities of up to 1 000 000 and 500 000 $cm^2/(V\ s)$ respectively,[5−10] suggesting that the intrinsic disorder in exfoliated graphene can be extremely low. Yet the mobility in graphene samples on SiO_2 substrates appears limited to ∼25 000 $cm^2/(V\ s)$.[11−13] The reason for this discrepancy remains the subject of some debate[14−19] with charged impurities in the SiO_2 substrate,[14,20−24] corrugations of graphene on rough SiO_2,[25−27] and resonant scatterers[28,29] proposed to explain the disorder. Charged impurities near the graphene sheet can explain the observed linear dependence of conductivity σ on carrier density n,[22] and there is consensus[15] that the observed magnitude of carrier density inhomogeneity in graphene[30,31] and the minimum conductivity at nominally zero carrier density σ_{min}[20,21] are determined by charged impurity disorder. However, the only attempt of which we are aware to characterize the charge disorder in graphene as well as the bare SiO_2 substrate concluded that charge variation in the substrate could not account for that observed in the graphene,[32] though we find that the analysis of the data is inconsistent with our observation as we will discuss below. Attempts to resolve the issue through transport experiments alone have been controversial, for instance, measurements of the dependence of graphene's conductivity on the dielectric constant of the environment,[14,16,17] and the ratio of the momentum scattering time to quantum scattering time[18,19] have produced conflicting results. The phenomenological observation of higher mobility for graphene suspended or on h-BN compared to SiO_2 is not conclusive since there could be a number of competing effects such as charged impurities in SiO_2, chemical hybridization of graphene with dangling bonds in SiO_2 which could lead to resonant scatterers,[33] or corrugations of graphene on rough SiO_2.[34]

Here we use Kelvin probe force microscopy to directly measure the potential disorder in two common substrates used

Received: April 8, 2013
Revised: July 12, 2013
Published: July 23, 2013

   dx.doi.org/10.1021/nl4012529 | *Nano Lett.* 2013, 13, 3576−3580

for graphene devices, amorphous SiO_2 and h-BN, to provide an insight into charge inhomogeneity in these substrates. We analyze the autocorrelation function of the local potential distribution for distinct SiO_2 samples and find it is well described by a two-dimensional (2D) random distribution of charges at the surface, allowing us to determine the surface trapped charge density in a given sample to within a few percent. We find a significant variation of the magnitude of the trapped charge density between similarly prepared samples with values ranging from 0.24 to 2.7 × 10^{11} cm^{-2}, suggesting an uncontrolled environmental effect on the trapped charge density at the SiO_2 surface. Samples of h-BN on SiO_2 showed similar variation and were less well modeled by randomly distributed charges in a 2D plane. However h-BN on SiO_2 samples all showed significantly lower surface potential fluctuations than the cleanest SiO_2 samples supporting the hypothesis that lower surface potential fluctuations are related to the higher mobility in graphene on h-BN compared to SiO_2. In an attempt to understand the sample-to-sample variations in trapped charge density, we also address the effect of device fabrication conditions; in particular, we show that even small electron beam dosing can produce large (~2 × 10^{11} cm^{-2}) metastable trapped charge densities on SiO_2, and smaller charge densities on h-BN, and that annealing can reverse the effect of electron beam exposure. We propose that the metastable trapped charge after electron beam exposure reveals the density of deep traps at the SiO_2 surface, and these traps are responsible for the low charge carrier mobility observed in graphene on SiO_2. We expect our technique and analysis methods will be useful to assess the quality of other candidate substrates for graphene and other self-assembled electronic materials.

The substrates used in this work were fabricated as follows. Amorphous SiO_2 (300 nm) was grown on Si by dry thermal oxidation. We examined samples from two sources which are nominally identical to those used in refs 11 and 13. Si/SiO_2 (300 nm) samples were cleaved in ambient conditions and subsequently subjected to a moderate temperature chamber bake at 130 °C in vacuum (10^{-10} Torr). In order to best match the sample fabrication conditions for much of the exfoliated graphene/SiO_2/Si transport literature (often mechanically exfoliated in ambient conditions),[1,35] no additional cleaning was performed prior to imaging. h-BN was exfoliated from single crystals onto SiO_2 as described in ref 7. Simultaneous noncontact atomic force microscopy (NC-AFM) and Kelvin probe force microscopy (KPFM) were obtained as follows: images were acquired utilizing a UHV-AFM system (JEOL JSPM-4500A) and a Pt-coated Si cantilever with a nominal radius of curvature r_{tip} = 30 nm (nominal spring constant k = 40 N/m). In conjunction with the traditional AFM topographic feedback loop at the cantilever resonance (~300 kHz), a second feedback loop was established based on a low frequency alternating current (ac) bias signal (500 Hz, 200−500 mV) applied to the tip for the KPFM measurements. For each data point, the dc bias is adjusted to minimize the contact potential difference, producing the KPFM potential map. Simultaneous topographic imaging with KPFM feedback has the additional benefit of minimizing the electrostatic contribution to the force gradient such that the AFM accurately records topography. Scans are typically 1 μm^2 and 256 × 256 pixels and are taken at slow speeds (~2 h/scan). Subsequent scans from the same location exhibit a high degree of consistency in the potential distribution and indicate minimal drift in the Kelvin signal within the resolution limits of the instrument (on the order of 1−2 mV/hour).

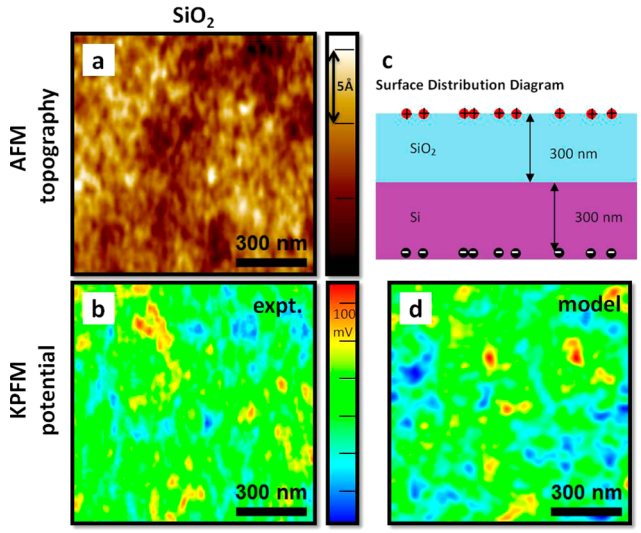

Figure 1. (a) Topography and (b) relative potential for the bare SiO_2/Si substrate. (c) Model of the expected charge distribution. (d) Potential for a simulated charge distribution (parameters are charge density n_{imp} = 2.5 × 10^{11} cm^{-2}, distance of tip to charges d = 1 nm, oxide thickness d_{ox} = 300 nm). Color scale in (d) is same as (b) with full range of 630 mV.

Figure 1 shows the topography and surface potential of a typical SiO_2/Si substrate (frequency shift Δf = −100 Hz, amplitude A = 5.0 nm). The topographic variations (Figure 1a) are consistent with those reported elsewhere, though the spatial resolution of the metal-coated AFM tip is insufficient to resolve the finest features.[34] Figure 1b shows the surface potential of the same area in Figure 1a. The surface potential shows variations that are not explicitly correlated with the topography (Figure 1a). In order to explain the observed random potential variation, we develop a model for the surface potential as follows. We first assume that the charges are primarily at the surface of the SiO_2 substrate, hence we use a two-dimensional random distribution of charges of density n_{imp} to model the expected potential distribution. We then assume that the tip measures the potential in a plane at a fixed distance d above the sample. Because of the presence of the highly conducting silicon ground plane a distance d_{ox} = 300 nm below the SiO_2 surface, the potential of a given charge is the sum of its Coulomb potential and that of its image, located $2d_{ox}$ = 600 nm below the charge. Figure 1c shows this schematically. We treat the charges as embedded in a uniform half-plane of effective dielectric constant $\varepsilon_r = (1 + \varepsilon_{SiO2})/2 \approx 2.45$ where ε_{SiO2} = 3.9 is the dielectric constant of SiO_2; this gives an exact result for the potential in the plane of the charges at the interface of SiO_2 and vacuum and is an excellent approximation for our geometry. Figure 1d shows the potential obtained from the model using n_{imp} = 2.5 × 10^{11} cm^{-2} and d = 1 nm. The potential is convoluted with a Gaussian of fwhm = r_{tip} = 30 nm to account for broadening due to the finite tip size. Although a full understanding of Kelvin probe imaging of semiconducting surfaces requires more complex models of the tip,[36−39] this simple Gaussian convolution approach nonetheless provides a valuable qualitative result. The model potential shows very similar variation in magnitude and spatial dimension to the experimentally obtained potential map (Figure 1c). These

dx.doi.org/10.1021/nl4012529 | Nano Lett. 2013, 13, 3576−3580

images are shown with the same potential scale for ready comparison. While this simulation provides a useful qualitative comparison, a more detailed quantitative comparison of the statistical properties of the simulated and experimental potentials is made below.

Previous analysis of the surface potential of SiO_2 examined the variance of the potential.[32] However, because the potential of a Coulomb impurity diverges at small distances as $1/r$, the experimentally observed variance of the potential depends critically on the cutoff length scales in the experimental measurement (i.e., d and r_{tip} discussed above), which can remove the divergence of the impurity potential. In the previous scanning single electron transistor measurement,[32] d and r_{tip} were not explicitly known, but they were estimated to exceed 100 nm (comparable to d_{ox}). In our experiment, we quantitatively analyze the full 2D autocorrelation function of the potential $C(r)$, which gives the similarity of potential measurements as a function of the spatial separation r, rather than only the variance (equal to the value of the autocorrelation function at $r = 0$, $C(0)$). We fit the full $C(r)$ to a model of random charges in a 2D plane, allowing us to estimate the charge density n_{imp} and tip-charge distance d. Furthermore, the higher spatial resolution in our measurement allows us to probe $C(r)$ at distances $[d, r_{tip}] \ll r \ll d_{ox}$ where $C(r)$ depends overwhelmingly on the density of charges n_{imp} and is insensitive to the magnitude of d, r_{tip}. This limit thus provides a reliable experimental methodology to estimate n_{imp}.

An analytical form of the $C(r)$ for an infinite, 2D random distribution of point charges has been utilized previously to describe disorder in graphene[40−42] and semiconductor heterojunctions.[43,44] For uncorrelated charges, the multicharge $C(r)$ will be simply the product of the single point charge autocorrelation function $C_p(r)$ and the total number of charges N_{imp}: $C(r) = N_{imp}C_p(r)$. To account for the finite size limitations and sampling resolution of the experimentally obtained data, we find $C_p(r)$ numerically starting from a potential grid with same size and sampling resolution as the experimentally obtained images using the dipole potential of the charge and its image in the Si ground plane. Finally, to account for signal broadening due to the finite size of the tip, we convolve $C(r)$ with a Gaussian with a fwhm = r_{tip} = 30 nm. N_{imp} and d are extracted as fitting parameters from the least-squares fit. Dividing N_{imp} by the image area gives the charged impurity density, n_{imp}.

Figure 2 shows the autocorrelation function of the potential $C(r)$ for SiO_2/Si sample shown in Figure 1a,b. The $C(r)$ data from three images at distinct locations on the same sample were averaged; the error bars are given by the standard deviation of the averaging. The best fit of the model to the experimental $C(r)$ is also shown in Figure 2. The fit parameters are $n_{imp} = (2.7 \pm 0.1) \times 10^{11}$ cm^{-2} and d = 4.7 Å, a reasonable tip−sample distance for an AFM measurement. Although the model does not explicitly account for the cantilever oscillation, the tip−sample distance d is best understood as corresponding to an approximate minimum tip−sample distance (e.g., at the bottom of the cantilever oscillation). The short-range behavior of the autocorrelation function is determined by the tip−sample distance (d) and the tip-size broadening (r_{tip}), while the downturn at large r is determined by the finite system size (limited by the image size and explicitly accounted for by discrete, numerical approach used for the fitting described above). The fit for midranged distances (50 nm < r < 200 nm) depends primarily on n_{imp} which sets the overall vertical scale of

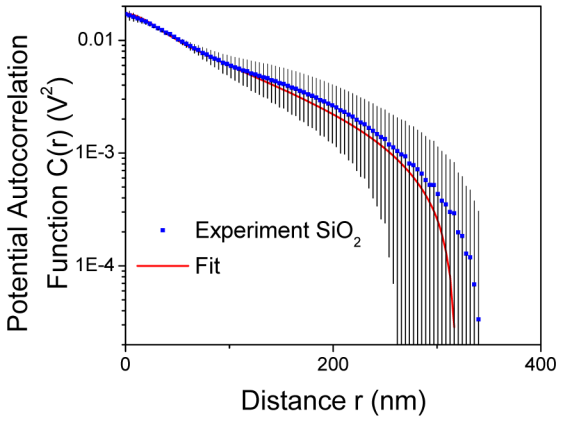

Figure 2. Autocorrelation function from experiment (blue squares, average from 3 images) and best theoretical fit ($n_{imp} = 2.7 \times 10^{11}$ cm^{-2}, d = 1 nm, d_{ox} = 300 nm). For the fit function, the autocorrelation function was convolved with a Gaussian of fwhm =30 nm to account for broadening due to the size of the tip.

$C(r)$. Variation of d and r_{tip} by a factor of 2 changes $C(r)$ by 2% in this region, allowing a highly accurate determination of n_{imp} independent of possible uncertainty in d and r_{tip}. We find a robust fit in this region within the 1.5 standard deviations for the five SiO_2 samples studied with n_{imp} values in the range $(0.24 \pm 0.01) \times 10^{11}$ cm^{-2} to $(2.7 \pm 0.1) \times 10^{11}$ cm^{-2}. The range represents the variation from sample to sample; much smaller variations are seen for different regions of a given sample. It is not clear whether the sample-to-sample variations are the result of variations between wafers (samples were obtained from different wafers) or due to an as-yet unidentified difference in processing conditions.

We now turn to the surface potential of exfoliated h-BN on SiO_2. Figure 3 shows the topography (Figure 3a) and surface

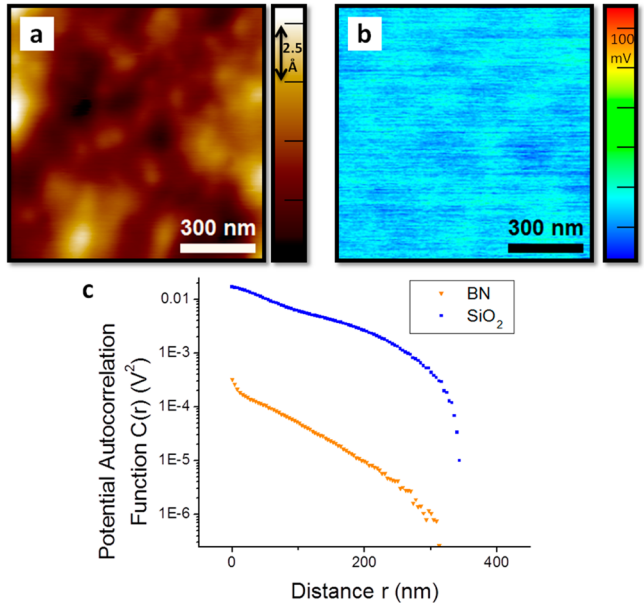

Figure 3. (a) Topographic and (b) potential images from a 40 nm h-BN flake exfoliated onto SiO_2. The same potential scale as used in Figure 1 is used for comparison (full range 630 mV). (c) The magnitude of the autocorrelation function for BN (orange triangles, average from nine images) is reduced from that for the underlying SiO_2 (blue squares, same as Figure 2).

dx.doi.org/10.1021/nl4012529 | Nano Lett. 2013, 13, 3576−3580

potential (Figure 3b) for a 40 nm thick h-BN flake on SiO_2/Si (frequency shift Δf = −70 Hz, amplitude A = 3.8 nm). Comparison with the samples on bare SiO_2/Si (Figure 1b) shows significantly lower potential variations for h-BN (Figures 1b and 3b utilize the same color scale). Similar to the SiO_2 samples, the h-BN samples showed strong decay of $C(r)$ as r increases. Shown in Figure 3 is $C(r)$ computed for one of the h-BN samples by taking an average of nine images from distinct areas. Comparing to the samples on SiO_2, $C(r)$ of the h-BN sample is almost 2 orders of magnitude lower. Although $C(r)$ in this particular h-BN sample is the lowest we measured, all other h-BN samples showed $C(r)$ lower than the cleanest samples on SiO_2. Of the three h-BN flakes measured, one showed $C(r)$ magnitude comparable to the one reported here and the other showed $C(r)$ magnitude ∼10× greater than the one reported here (though still lower than the lowest $C(r)$ observed on SiO_2), though this third flake exhibited topographic features and region-to-region inconsistency in the potential distribution not observed in the other flakes, which may indicate that the data for this particular flake is an unreliable metric for understanding charged impurity density in h-BN substrates. We note that the curve shape of $C(r)$ of the h-BN samples is not explained by our simple 2D charge trap model presented above, for any d. However, the lower magnitude of $C(r)$ for h-BN compared to SiO_2, which indicates reduced potential fluctuations, suggests that reduced potential/density inhomogeneity is responsible for increase in the maximum mobility limited by charged impurity scattering observed for graphene on h-BN compared to SiO_2.

A more complete understanding of the link between charged impurities in the substrate and device mobility requires consideration of common graphene fabrication conditions. Here we address the effects of electron beam lithography and annealing by dosing as fabricated substrates in situ with an electron beam using a scanning electron microscope (SEM) for 30 s. Figure 4 shows the charge density as a function of time after SEM exposure for h-BN [initial n_{imp} = 2.5 × 10^9 cm^{-2}] and a clean SiO_2 sample [initial n_{imp} = (0.24 ± 0.01) × 10^{11} cm^{-2}]. The n_{imp} values in Figure 4 were obtained from the value of $C(r)$ at r = 50 nm. On the basis of beam parameters, image size, and dosing time we expect the total electron exposure is on the order of 10^{11}−10^{12} cm^{-2}, consistent with the charge densities observed immediately after dosing. This dose is comparable to or lower than the minimum order expected during standard graphene device fabrication by electron beam lithography where we estimate that an electron dose of at least order 10^{12} cm^{-2} results from unintentional exposure while locating and aligning to existing patterns on the substrate; the dose in the intentionally exposed contact areas is much higher, on the order of 10^{15} cm^{-2}. Thus the behavior observed in Figure 4 from our samples is indicative of realistic fabrication conditions. The SiO_2 appears to reach a metastable state 8 h after electron-beam dosing with charged impurity density of ∼2 × 10^{11} cm^{-2} while the h-BN did not show evidence of metastable charge density greater than 5 × 10^{10} cm^{-2}. Both SiO_2 and h-BN return to close to their initial state after 30 min of heating at ∼250−300 °C, though h-BN appears to be less reversible. Some research groups have adopted the practice of annealing graphene in a reducing environment post lithography in order to remove resist residues;[45] our results suggest the possibility that annealing may have the additional benefit of removing metastable trapped charge induced by electron-beam processing, though our annealing conditions (UHV) are not typical.

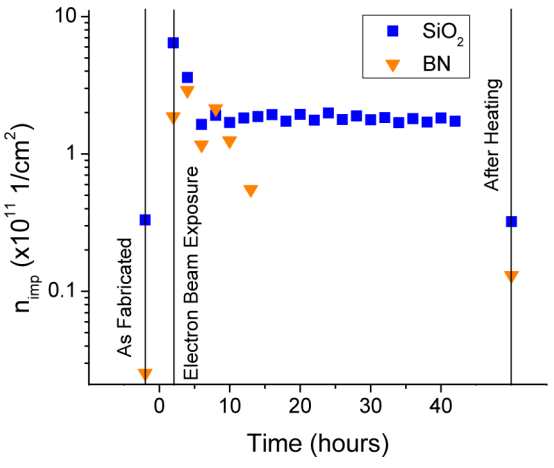

Figure 4. Effect of fabrication procedures (electron beam exposure and annealing) on graphene substrate charged impurity density. The surface charge densities before electron beam exposure, as a function of time after electron beam exposure and after annealing at 250 C are shown for SiO_2 (blue squares) and h-BN (orange triangle) substrates.

We now discuss the implications of our results for understanding the disorder-limited charge carrier mobilities observed for graphene on SiO_2 and h-BN substrates. A previous study[24] used controlled adsorption of potassium (a charged impurity on graphene) to determine the relationship between charged impurity density n_{imp} and charge carrier mobility μ in graphene: μ = 5 × 10^{15} $V^{-1}s^{-1}/n_{imp}$. The best measured mobilities for graphene on SiO_2 are ∼25,000 $cm^2/(V\ s)$[11−13] implying charge trap densities of ∼2 × 10^{11} cm^{-2} or more. Moreover, scanning probe studies from several groups show consistent results for the potential fluctuations in graphene on SiO_2 (electron and hole "puddles") with root mean square charge variations of (2−4) × 10^{11} cm^{-2}.[30−32] Thus there is significant evidence that charge trap densities seen by graphene on SiO_2 are at least ∼2 × 10^{11} cm^{-2}. Our experimentally determined n_{imp} = 0.24 − 2.7 × 10^{11} cm^{-2} for SiO_2 samples encompasses the expected range inferred from these previous experiments. However, it is difficult to understand the cleanest samples (with n_{imp} = 0.24 × 10^{11} cm^{-2}), which are seemingly inconsistent with previous inferred substrate charge density results for graphene on SiO_2. We believe the solution to this conundrum is offered by the electron-beam dosing results. We find that long-lived charge densities of ∼2 × 10^{11} cm^{-2} can be induced in the cleanest SiO_2, implying that the density of deep trap states at the SiO_2 surface is at least this large. We hypothesize that the presence of conducting graphene fills these deep trap states through tunneling and thus trapped charge densities of ∼2 × 10^{11} cm^{-2} are unavoidable at the SiO_2/graphene interface. An additional possibility is that ambient species adsorbed between graphene and SiO_2 during deposition may act as charge traps.[30,32,46−48]

For h-BN, we consistently observe lower potential fluctuations than for SiO_2 and also lower metastable trapped charge densities. The results support the hypothesis that lower trapped charge densities in h-BN are responsible for the higher disorder-limited charge carrier mobility for graphene on h-BN compared to SiO_2. The potential fluctuations on h-BN are often poorly fit by our model of random charges in a 2D plane. More

dx.doi.org/10.1021/nl4012529 | Nano Lett. 2013, 13, 3576−3580

work is needed to understand the details of the charge distribution, including its depth dependence and correlations.

In conclusion, we have used Kelvin probe force microscopy to map the surface potential of both SiO_2/Si and h-BN substrates. We analyze the experimental potential autocorrelation function of the substrates and compare to a numerical model of charges randomly distributed in a 2D plane. For SiO_2/Si, we have observed charged impurity densities in individual samples of n_{imp} = 0.24 - 2.7 × 10^{11} cm^{-2}. h-BN substrates show improvement in potential inhomogeneity over SiO_2, consistent with the observed improvement in mobility for graphene devices on h-BN. Electron beam dosing creates metastable charge trap populations of a few 10^{11} cm^{-2} which can be removed by annealing at 250 °C. The observation of metastable charge trap populations on the surface of SiO_2 with concentrations of a few 10^{11} cm^{-2} is strongly suggestive that such charge traps, filled by device processing or simply by contact with conducting graphene, are responsible for the scattering and charge-carrier inhomogeneity in graphene on SiO_2. We expect our technique and analysis methods can be generally useful to assess the quality of new substrates for graphene or other self-assembled materials.

AUTHOR INFORMATION

Corresponding Author

*E-mail: wcullen@umd.edu.

Notes

The authors declare no competing financial interest.

ACKNOWLEDGMENTS

This work was supported by the University of Maryland NSF-MRSEC under Grant DMR 05-20471 and the U.S. ONR MURI program. S.A. is supported by the National Research Foundation Singapore under its Fellowship program (NRF-NRFF2012-01).

REFERENCES

(1) Geim, A. K.; Novoselov, K. S. *Nat. Mater.* **2007**, *6*, 183−191.

(2) Novoselov, K. S.; Geim, A. K.; Morozov, S. V.; Jiang, D.; Zhang, Y.; Dubonos, S. V.; Grigorieva, I. V.; Firsov, A. A. *Science* **2004**, *306*, 666−669.

(3) Castro Neto, A. H.; Guinea, F.; Peres, N. M. R.; Novoselov, K. S.; Geim, A. K. *Rev. Mod. Phys.* **2009**, *81*, 109.

(4) Chen, J.-H.; Jang, C.; Xiao, S.; Ishigami, M.; Fuhrer, M. S. *Nat. Nanotechnol.* **2008**, *3*, 206−209.

(5) Du, X.; Skachko, I.; Barker, A.; Andrei, E. Y. *Nat. Nanotechnol.* **2008**, *3*, 491−495.

(6) Bolotin, K. I.; Sikes, K. J.; Hone, J.; Stormer, H. L.; Kim, P. *Phys. Rev. Lett.* **2008**, *101*, 096802.

(7) Dean, C. R.; Young, A. F.; Meric, I.; Lee, C.; Wang, L.; Sorgenfrei, S.; Watanabe, K.; Taniguchi, T.; Kim, P.; Shepard, K. L.; Hone, J. *Nat. Nanotechnol.* **2010**, *5*, 722−726.

(8) Mayorov, A. S.; Gorbachev, R. V.; Morozov, S. V.; Britnell, L.; Jalil, R.; Ponomarenko, L. A.; Blake, P.; Novoselov, K. S.; Watanabe, K.; Taniguchi, T.; Geim, A. K. *Nano Lett.* **2011**, *11*, 2396−2399.

(9) Castro, E. V.; Ochoa, H.; Katsnelson, M. I.; Gorbachev, R. V.; Elias, D. C.; Novoselov, K. S.; Geim, A. K.; Guinea, F. *Phys. Rev. Lett.* **2010**, *105*, 266601.

(10) Zomer, P. J.; Dash, S. P.; Tombros, N.; van Wees, B. J. *Appl. Phys. Lett.* **2011**, *99*, 232104−232104−3.

(11) Tan, Y.-W.; Zhang, Y.; Bolotin, K.; Zhao, Y.; Adam, S.; Hwang, E. H.; Das Sarma, S.; Stormer, H. L.; Kim, P. *Phys. Rev. Lett.* **2007**, *99*, 246803.

(12) Cho, S.; Fuhrer, M. S. *Phys. Rev. B* **2008**, *77*, 081402.

(13) Yan, J.; Fuhrer, M. S. *Phys. Rev. Lett.* **2011**, *107*, 206601.

(14) Jang, C.; Adam, S.; Chen, J.-H.; Williams, E. D.; Das Sarma, S.; Fuhrer, M. S. *Phys. Rev. Lett.* **2008**, *101*, 146805.

(15) Ni, Z. H.; Ponomarenko, L. A.; Nair, R. R.; Yang, R.; Anissimova, S.; Grigorieva, I. V.; Schedin, F.; Blake, P.; Shen, Z. X.; Hill, E. H.; Novoselov, K. S.; Geim, A. K. *Nano Lett.* **2010**, *10*, 3868−3872.

(16) Ponomarenko, L. A.; Yang, R.; Mohiuddin, T. M.; Katsnelson, M. I.; Novoselov, K. S.; Morozov, S. V.; Zhukov, A. A.; Schedin, F.; Hill, E. W.; Geim, A. K. *Phys. Rev. Lett.* **2009**, *102*, 206603.

(17) Newaz, A. K. M.; Puzyrev, Y. S.; Wang, B.; Pantelides, S. T.; Bolotin, K. I. *Nat. Commun.* **2012**, *3*, 734.

(18) Monteverde, M.; Ojeda-Aristizabal, C.; Weil, R.; Bennaceur, K.; Ferrier, M.; Guéron, S.; Glattli, C.; Bouchiat, H.; Fuchs, J. N.; Maslov, D. L. *Phys. Rev. Lett.* **2010**, *104*, 126801.

(19) Hong, X.; Zou, K.; Zhu, J. *Phys. Rev. B* **2009**, *80*, 241415.

(20) Rossi, E.; Adam, S.; Das Sarma, S. *Phys. Rev. B* **2009**, *79*, 245423.

(21) Adam, S.; Hwang, E. H.; Galitski, V. M.; Das Sarma, S. *Proc. Natl. Acad. Sci. U.S.A.* **2007**, *104*, 18392−18397.

(22) Hwang, E. H.; Adam, S.; Das Sarma, S. *Phys. Rev. Lett.* **2007**, *98*, 186806.

(23) Rossi, E.; Das Sarma, S. *Phys. Rev. Lett.* **2008**, *101*, 166803.

(24) Chen, J.-H.; Jang, C.; Adam, S.; Fuhrer, M. S.; Williams, E. D.; Ishigami, M. *Nat. Phys.* **2008**, *4*, 377−381.

(25) Kim, E.-A.; Castro Neto, A. H. *EPL* **2008**, *84*, 57007.

(26) Katsnelson, M. I.; Geim, A. K. *Philos. Trans. R. Soc. London, Ser. A* **2008**, *366*, 195−204.

(27) Gibertini, M.; Tomadin, A.; Polini, M.; Fasolino, A.; Katsnelson, M. I. *Phys. Rev. B* **2010**, *81*, 125437.

(28) Wehling, T. O.; Yuan, S.; Lichtenstein, A. I.; Geim, A. K.; Katsnelson, M. I. *Phys. Rev. Lett.* **2010**, *105*, 056802.

(29) Stauber, T.; Peres, N. M. R.; Guinea, F. *Phys. Rev. B* **2007**, *76*, 205423.

(30) Zhang, Y.; Brar, V. W.; Girit, C.; Zettl, A.; Crommie, M. F. *Nat. Phys.* **2009**, *5*, 722−726.

(31) Deshpande, A.; Bao, W.; Miao, F.; Lau, C. N.; LeRoy, B. J. *Phys. Rev. B* **2009**, *79*, 205411.

(32) Martin, J.; Akerman, N.; Ulbricht, G.; Lohmann, T.; Smet, J. H.; Klitzing, K. von; Yacoby, A. *Nat. Phys.* **2007**, *4*, 144−148.

(33) Kang, Y.-J.; Kang, J.; Chang, K. J. *Phys. Rev. B* **2008**, *78*, 115404.

(34) Cullen, W. G.; Yamamoto, M.; Burson, K. M.; Chen, J. H.; Jang, C.; Li, L.; Fuhrer, M. S.; Williams, E. D. *Phys. Rev. Lett.* **2010**, *105*, 215504.

(35) Novoselov, K. S.; Jiang, D.; Schedin, F.; Booth, T. J.; Khotkevich, V. V.; Morozov, S. V.; Geim, A. K. *Proc. Natl. Acad. Sci. U.S.A.* **2005**, *102*, 10451−10453.

(36) Sadeghi, A.; Baratoff, A.; Ghasemi, S. A.; Goedecker, S.; Glatzel, T.; Kawai, S.; Meyer, E. *Phys. Rev. B* **2012**, *86*, 075407.

(37) Rosenwaks, Y.; Shikler, R.; Glatzel, T.; Sadewasser, S. *Phys. Rev. B* **2004**, *70*, 085320.

(38) Hudlet, S.; Saint Jean, M.; Roulet, B.; Berger, J.; Guthmann, C. *J. Appl. Phys.* **1995**, *77*, 3308−3314.

(39) Ludeke, R.; Cartier, E. *Microelectron. Eng.* **2001**, *59*, 259−263.

(40) Das Sarma, S.; Adam, S.; Hwang, E. H.; Rossi, E. *Rev. Mod. Phys.* **2011**, *83*, 407−470.

(41) Galitski, V. M.; Adam, S.; Das Sarma, S. *Phys. Rev. B* **2007**, *76*, 245405.

(42) Adam, S.; Jung, S.; Klimov, N. N.; Zhitenev, N. B.; Stroscio, J. A.; Stiles, M. D. *Phys. Rev. B* **2011**, *84*, 235421.

(43) Efros, A. L.; Pikus, F. G.; Burnett, V. G. *Phys. Rev. B* **1993**, *47*, 2233−2243.

(44) Ando, T.; Fowler, A. B.; Stern, F. *Rev. Mod. Phys.* **1982**, *54*, 437−672.

(45) Ishigami, M.; Chen, J. H.; Cullen, W. G.; Fuhrer, M. S.; Williams, E. D. *Nano Lett.* **2007**, *7*, 1643−1648.

(46) Xu, K.; Cao, P.; Heath, J. R. *Science* **2010**, *329*, 1188−1191.

(47) Leenaerts, O.; Partoens, B.; Peeters, F. M. *Phys. Rev. B* **2008**, *77*, 125416.

(48) Zhao, J.; Buldum, A.; Han, J.; Lu, J. P. *Nanotechnology* **2002**, *13*, 195.